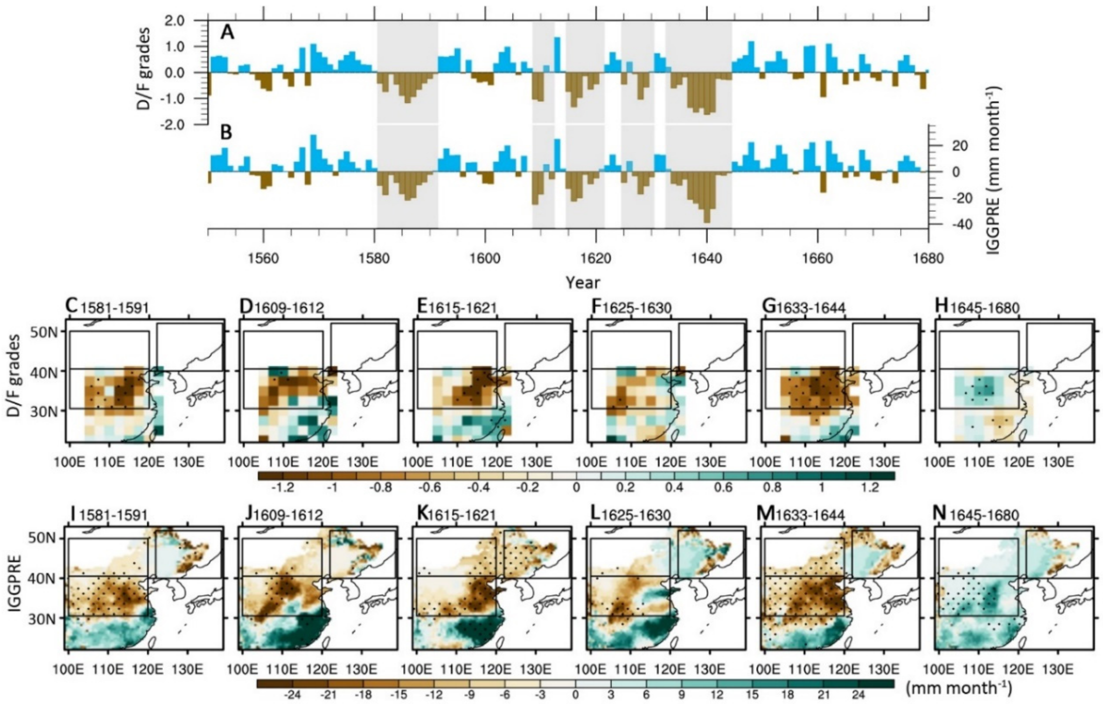

Figure S1. Dry-wet conditions over North and Northeast China during 1550-1680 from the IGGPRE and Drought/flood (D/F) grades datasets. a D/F grades over North China[24]. **b** Precipitation anomalies (mm month^{-1}) over North China, relative to 1500–2000, from the IGGPRE[25]. Grey shadings mark the five droughts in North China. (**c**–**g**) The spatial patterns of precipitation anomalies (mm month^{-1}) from the IGGPRE during each of the five drought events highlighted in Figure 1 and 1581–1644. **h** Dry-wet conditions during the early Qing period under Manchu rule (1645–1680). (**i**–**n**) are the same as (**c**–**h**), but for the results from the D/F grades dataset. Stippling denotes the significance at the 90% confidence level (two-tailed Student's t-test).

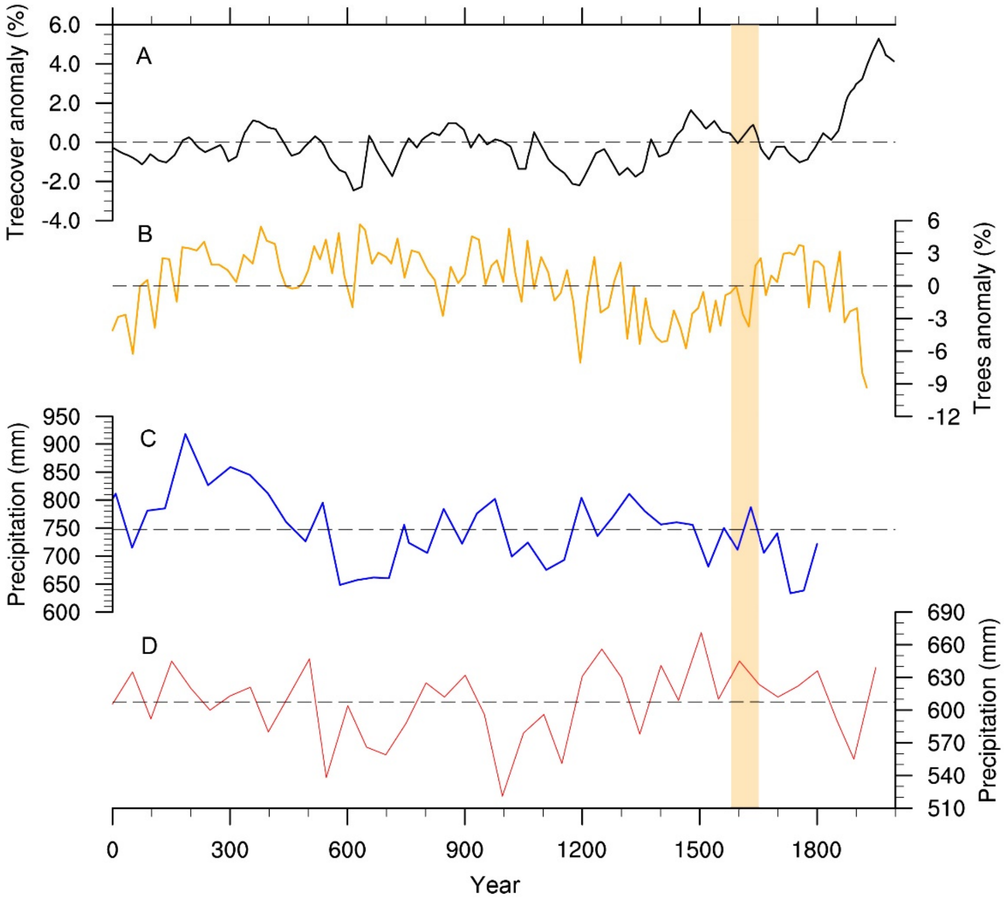

Figure S2. Vegetation and hydroclimate changes in Northeast China. a Tree cover anomaly in the central-northern parts of the Daxing'an Mountains[26]. **b** Trees anomaly in the Lake Xiaolongwan[27] (42°18′N, 126°21′E). **c** Pollen-based mean annual precipitation anomaly in the Lake Sihailongwan[28] (42°17’N, 126°36’E). **d** Peat GST[29] in the northernmost EASM region. Horizontal dashed lines represent the long-term mean value over the past two millennium in each data.

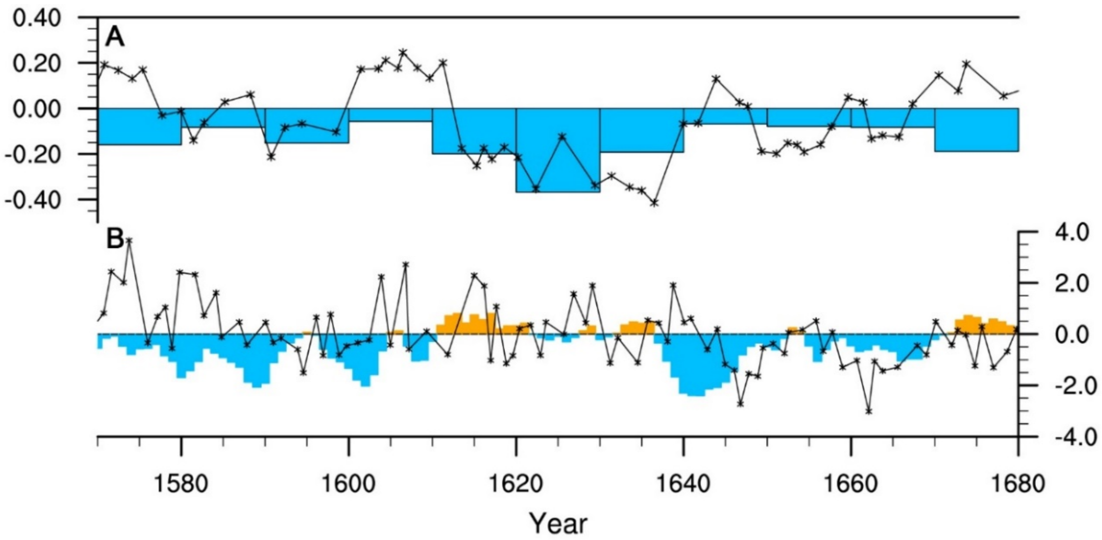

Figure S3. Temperature changes over North and Northeast China during the Ming-Qing transition. a Decadal temperature anomalies (°C) over North China[3] (blue charts) and extreme cold wave events in southern China[75] (black line). **b** Tree-ring-based winter temperature averaged over Northeast China[76] (charts) and minimum temperatures of the autumn-winter season (°C) in Northeast Asia[77] (black line).

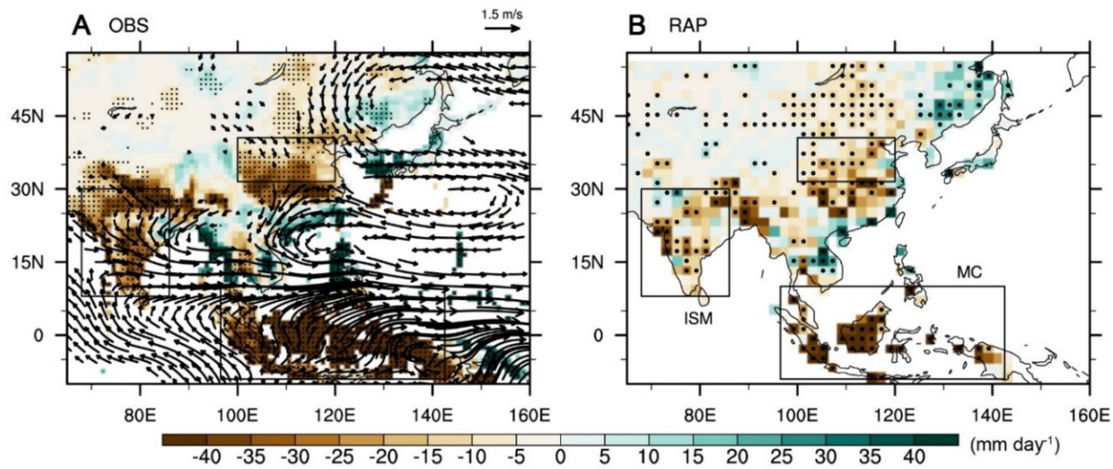

Figure S4. Observed and reconstructed Asian summer precipitation in response to ENSO during the period of 1901-2010. JJA mean precipitation anomalies (mm month^{-1}) between the composite El Niño and La Niña events in the ENSO developing years derived from the GPCC observation (**a**) and RAP reconstruction (**b**). Vectors in (**a**) represent the 850-hPa winds anomalies (m s^{-1}). Black boxes represent regions of NC, ISM, and MC, respectively. Stippling denotes the significance at the 90% confidence level (two-tailed Student's t-test).

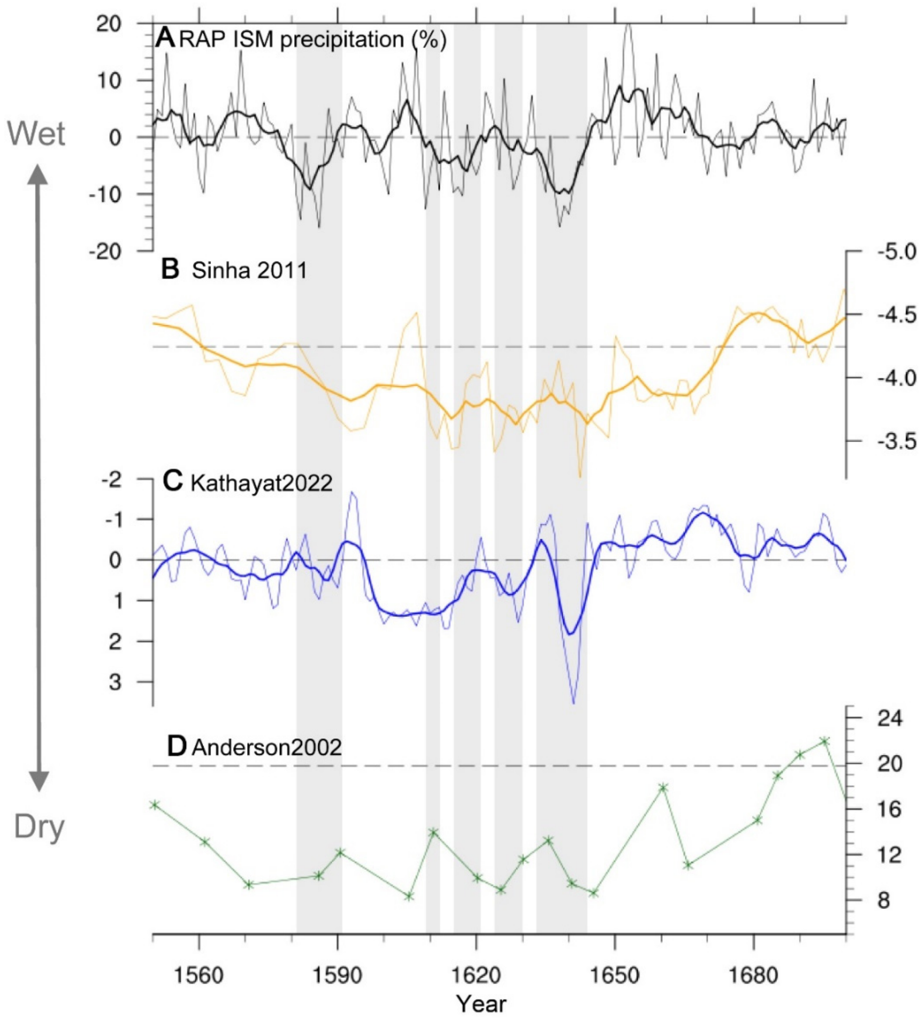

Figure S5. Comparison of the Indian summer monsoon reconstructions during 1550-1700. a Percentage changes in the Indian summer monsoon precipitation (%) derived from the RAP[23]. **b** The near annually resolved speleothem $\delta^{18}O$ record from Jhumar Cave located in central India[48]. **c** The detrended z-score-transformed speleothem $\delta^{18}O$ record from Mawmluh cave located in northeast India[49]. Thick lines in (**a**–**c**) represent the 7-point running-mean results. **d** A marine record of upwelling intensity from the Arabian Sea[47]. Horizontal dashed lines represent the long-term mean value over the past millennium in each data.

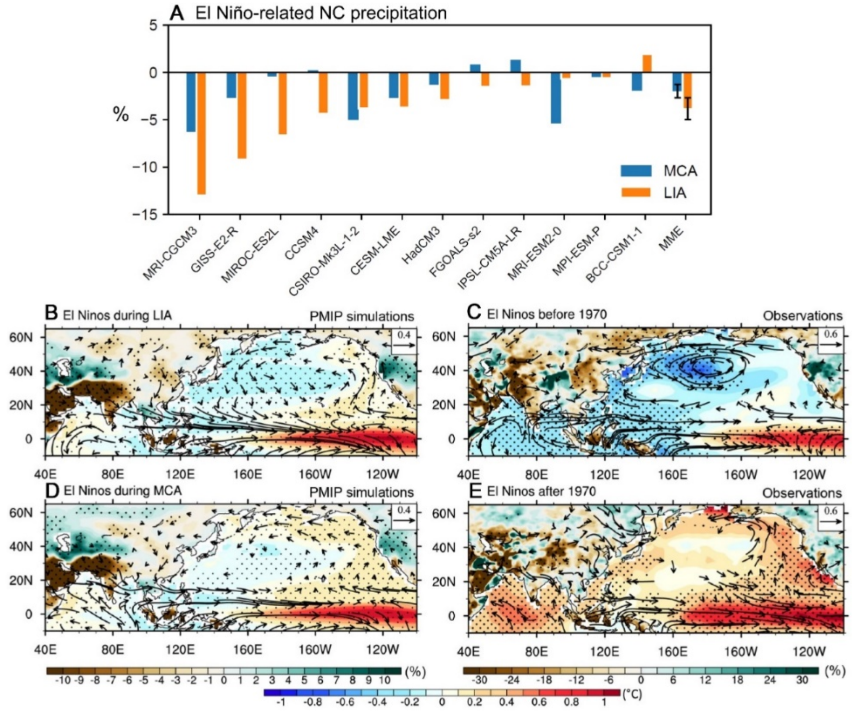

Figure S6. Impacts of El Niño on the North China climate under warm and cold climate conditions. **a** Percentage changes in JJA precipitation over North China averaged for El Niño developing years during the MCA (950–1200, blue) and LIA (1600–1850, orange). Error bars on the multi-model mean (MME) are calculated as 1.0 s.d. of 10,000 inter-realizations of a bootstrap method. **b** Simulated JJA mean SST and 850-hPa winds anomalies (m s^{-1}) and percentage changes in land precipitation averaged for El Niño events during the LIA (1600–1850) and (**c**) MCA (950–1200) from 12-model simulations of the PMIP and CESM-LME. **d** Observed JJA mean SST and 850-hPa winds anomalies (m s^{-1}) and percentage changes in land precipitation averaged for El Niño events during 1901–1970 and (**e**) 1971–2020. The stippled areas denote regions where more than 70% of the individual models agree on the sign. Only the significant 850-hPa wind anomalies are displayed.

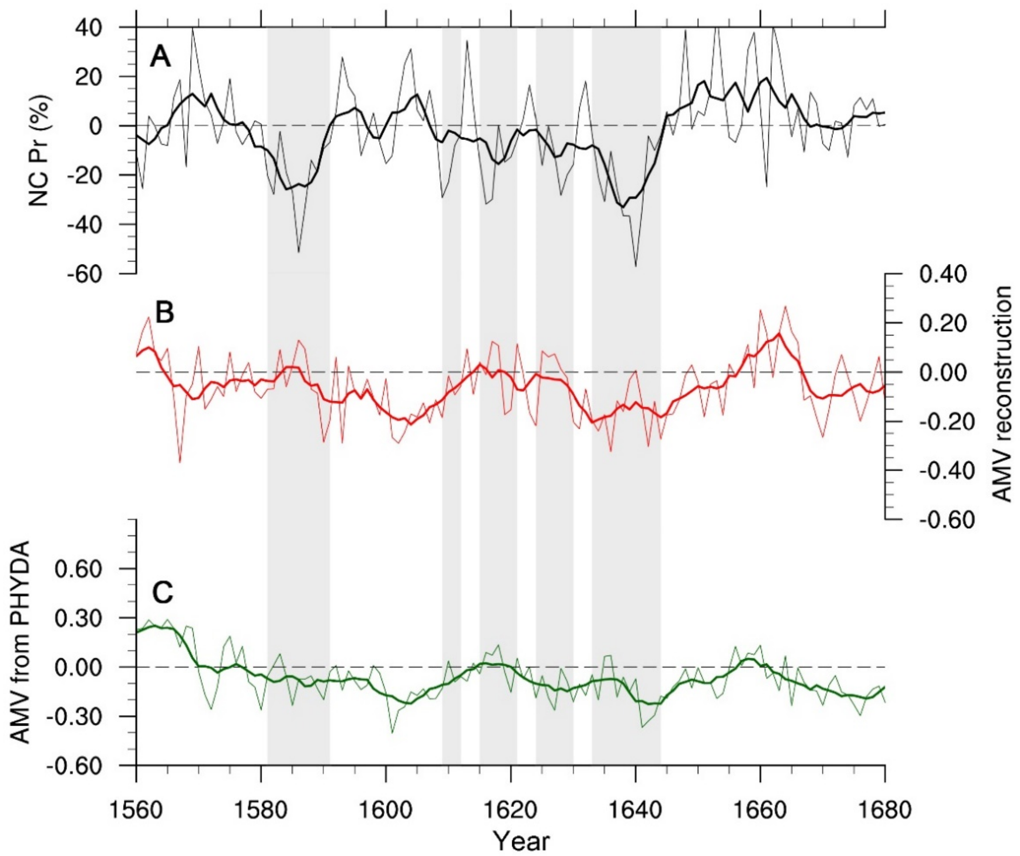

Figure S7. Evolutions of main internal climate modes on the decadal time scale during the late Ming dynasty. a Percentage changes in precipitation (%) over North China in the RAP[23]. **b** AMV reconstruction from Wang et al.[61]. **c** Reconstructed JJA mean AMV derived from PHYDA[42]. Thick lines represent results after a 7-year running mean. Horizontal dashed lines represent the long-term mean value over the past millennium in each data.

Table S1. The major battles between the Ming and Manchu shown in Fig. 3d.

Time	Major battles	Results
1618–1619	Sarhu	Manchus prevails
1621	Shenyang, Liaoyang, and Fushun	Manchus prevails
1626	Ningyuan	Ming prevails
1627	Jinzhou	Ming prevails
1629	Beijing	Ming prevails
1631	Daling River	Manchus prevails
1634	Datong	Manchus prevails
1636–1637	Qing invasion of Joseon	Manchus prevails
1638–1639	The Qing attacked many cities in Shanxi and Shandong	Manchus prevails
1641–1642	Song-Jin	Manchus prevails
1644	Shanhai Pass	Manchus prevails

Table S2. Last-millennium simulations from the PMIP3/4 and CESM-LME.

Model	Volcanic forcing	Solar forcing	Period	Project
BCC-CSM-1.1	GRA	VSK+WLS back	850-2000	PMIP3
CCSM4	GRA	VSK	850-2005	PMIP3
CSIRO-Mk3L-1.2	CEA	SBF	851-2000	PMIP3
FGOALS-s2	GRA	VSK+WLS back	850-2005	PMIP3
GISS-E2-R	CEA	SBF/VSK+WLS back	850-2005	PMIP3
HadCM3	CEA	SBF+WLS back	850-2005	PMIP3
IPSL-CM5A-LR	Ammann	VSK+WLS back	850-2005	PMIP3
MPI-ESM-P	CEA	VSK+WLS back	850-2005	PMIP3
MRI-CGCM3	GRA	DB back+WLS back	850-2005	PMIP3
MIROC-ES2L	Toohey	BU	850-2014	PMIP4
MRI-ESM2-0	Toohey	BU	850-2014	PMIP4
CESM-LME	GRA	VSK	850-2005	LME

GRA: Gao,et al. ; CEA: Crowley, et al. ; Toohey: Toohey and Sigl; VSK: Vieira, Krivova and Solanki; MEA: Muscheler, Joos, Beer, Müller, Vonmoos and Snowball; DB: Delaygue and Bard ; WLS: Wang, Lean and Sheely ; SBF: Steinhilber, Beer, and Frohlich; BU: Baroni et al. 2015 and Usoskin et al. 2016